Biosensors and Bioelectronics 77 (2016) 385–392

Contents lists available at ScienceDirect

Biosensors and Bioelectronics

journal homepage: www.elsevier.com/locate/bios

Real-time concentration monitoring in microfluidic system via plasmonic nanocrescent arrays

Bingpu Zhou [a,b], Xiao Xiao [b], Ting Liu [c], Yibo Gao [d], Yingzhou Huang [c], Weijia Wen [a,b,*]

[a] Nano Science and Technology Program and KAUST-HKUST Micro/Nanofluidic Joint Laboratory, The Hong Kong University of Science and Technology, Clear Water Bay, Kowloon, Hong Kong
[b] Department of Physics, The Hong Kong University of Science and Technology, Clear Water Bay, Kowloon, Hong Kong
[c] Soft Matter and Interdisciplinary Research Institute, College of Physics, Chongqing University, Chongqing 400044, China
[d] Environmental Science Programs, School of Science, The Hong Kong University of Science and Technology, Clear Water Bay, Kowloon, Hong Kong

ARTICLE INFO

Article history:
Received 20 July 2015
Received in revised form
3 September 2015
Accepted 23 September 2015
Available online 28 September 2015

Keywords:
Nanocrescent
Surface plasmon resonance
Microfluidics
Biosensor

ABSTRACT

In this work, on-chip bio/chemical sensor was reported based on localized surface plasmon resonance of nanocrescent patterns fabricated via electron beam lithography. The nanocrescent arrays with different dimensional features exhibited controllable plasmonic properties in accordance with the simulation results based on the finite-difference time-domain model. The highest refractive index sensitivity of the fabricated samples was achieved to be ~699.2 nm/RIU with a figure of merit of ~3.1 when the two opposite crescents own a gap of ~43.3 nm. Such obtained plasmonic sensor was further integrated into the microfluidic system which can simply control the specific analyte concentrations via tuning the flow rate ratios between two injecting microstreams. Our method has successfully demonstrated the capability of the nanocrescent patterns as on-chip plasmonic bio/chemical sensor for real-time monitoring of dynamic concentrations in the microchannel.

1. Introduction

Real-time probing of analyte concentration precisely in microfluidic systems is pivotal for characterizing various biological processes such as cell singaling, immune response, etc. (Ahmed et al., 2010; Fosser and Nuzzo, 2003; Xiao et al., 2013). As one of the most common techniques, microscopy has been proved to be efficient to produce information of on-chip bio/chemical concentrations (Mensack et al., 2013). However, the general requirement of fluorescent or chemiluminescent molecules in biological system limits its prominent application to some extent. Electrochemical sensing with integrated sensing electrodes in microfluidic channel is another well-employed approach for concentration monitoring (Gencoglu and Minerick, 2014; Yoon et al., 2014). The electrical contact between external power supply and the bioactive targets may unfortunately bring unrecoverable damages to the bio/chemical objects.

Among the numerous measuring approaches, optofluidics has been recently explored as an advanced method for on-chip bio/chemical assays (Schmidt and Hawkins, 2011). During the past decade, the combination of optics and microfluidics has served as a versatile platform for on-chip particle manipulation, imaging, or bio/chemical sensing, etc. (Erickson et al., 2011; Estevez et al., 2014; Pang et al., 2012). Localized surface plasmon resonance (LSPR) based on nano-particles or nano-patterns can significantly concentrate light into nano-scale region, which further effectively monitor the refractive index (RI) change of the medium close to the plasmonic surface (Stewart et al., 2008). To date, kinds of materials (gold, silver, etc.) and nano-patterns (prism, ring, crescent, etc.) have been well presented to be capable of sensing the RI based on the LSPR effect (Chen et al., 2008; Mannelli and Marco, 2010; Rycenga et al., 2011; Toma et al., 2014). However, rare demonstrations have been focused on adopting such plasmonic structures as integrated sensor in microfluidic system for real-time dynamic concentration monitoring (Huang et al., 2012; Escobedo et al., 2013).

Generating controllable bio/chemical concentrations in microfluidic system plays an important role in understanding complex biological aspects. One frequently used method is based on the intrinsic laminar characteristics of fluids in microscale with peripheral active or passive control (Ahmed et al., 2013; Jeon et al., 2000). In light of above, microfluidic system with capability of generating tunable concentrations as well as real-time probing is

* Corresponding author at: Nano Science and Technology Program and KAUST-HKUST Micro/Nanofluidic Joint Laboratory, The Hong Kong University of Science and Technology, Clear Water Bay, Kowloon, Hong Kong. Fax: +852 23581652.
E-mail address: phwen@ust.hk (W. Wen).

http://dx.doi.org/10.1016/j.bios.2015.09.054
0956-5663/

of great importance in the future complex on-chip bio/chemical processes. Limited research has yet concentrated on generation of dynamically controllable analyte concentrations combined with real-time on-chip effective and accurate concentration monitoring (Morel et al., 2012; Toetsch et al., 2009). In this work, we first designed and fabricated nanocrescent samples via electron beam lithography (EBL) with different geometries. Nanocrescent (NC) structure is one of the most common adopted plasmonic bio/chemical sensors due to the well-tunable LSPR property, highly confined electric field, etc. (Bukasov and Shumaker-Parry, 2007; Bukasov et al., 2010; Fischer et al., 2011). EBL was utilized to produce NC arrays with well controlled shapes and locations on the substrate which can facilitates ease of integration with the microfluidic system. The RI sensitivities were then systematically investigated and compared by using sodium chloride (NaCl) solution with different concentrations. Finally, one of the fabricated NC arrays was integrated into a microfluidic concentration gradient generator for real-time monitoring of dynamic analyte concentrations. The presented results are encouraging and convenient to be applied for on-chip monitoring of bio/chemical targets in the future.

2. Methods and materials

2.1. Design and fabrication of NC arrays

Fig. 1a illustrates the three-dimensional configuration of NC arrays patterned on a quartz substrate. It should be noted that here in the figure only paired NC arrays are depicted while in this work, both of single and paired NC were fabricated and investigated. P indicates the periodicity in both *X* (minor axis) and *Y* (major axis) directions between each individual NC unit. For the single and paired NC patterns, P is defined of 600 nm and the dimensional symbols for a NC unit are shown in Fig. 1b. *W* is the waist width of a single NC pattern and the gap between the tips of two opposite NC for the paired case is denoted as '*G*'.

Schematic of the fabrication process for NC patterns is provided in Fig. 1c. First, photoresist (ZEP-520A, Zeon Co. Ltd., Japan) was uniformly spin-coated onto a clean quartz wafer (Plan Optik, Germany), followed by EBL to accurately define the shapes of NC. After developing, 5 nm Ti (titanium) and 30 nm Au thin films were sequentially deposited onto the photoresist-patterned substrate. The bottom metal layer (Ti) here was adopted to enhance the adhesion between the top Au layer and the substrate. Finally, lift-off process was introduced to remove the photoresist residual together with the metals on top. Such fabrication process is also suitable for single NC patterns which are not described in the figure.

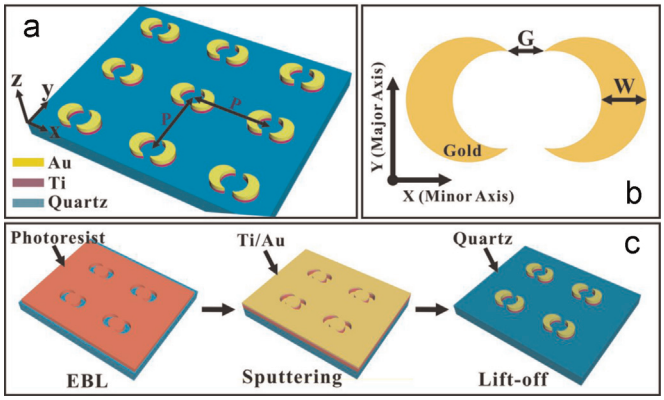

Fig. 1. (a) 3D configuration of NC arrays on a quartz substrate; (b) dimensional parameters of an individual NC unit; (c) fabrication process of paired NC arrays on a quartz substrate. The schematic is also suitable for fabrication of single NC patterns (not depicted in the figure).

2.2. Characterization of NC arrays

In this work, three different NC samples were fabricated on quartz substrate with well-defined morphologies and the covering area of the pattern array for each design is around 2 cm^2. For all NC arrays, the periodicity is set to be 600 nm in both of the major and minor axes. The top picture of Fig. 2a shows the atomic force microscope (AFM) image of sample S1 (single NC) and the enlarged scanning electron microscope (SEM) image that shows a waist width of around 111 nm. The AFM image also confirms the actual height of the NC that is corresponding to the processing parameters. SEM images of sample P2 and P3 (paired NC) are given which shows the different dimensional values of the two samples. For P2, *W* is around 86.3 nm and *G* is around 62.5 nm. For P3, *W* is slightly decreased to around 66.7 nm and *G* of around 43.3 nm. We can clearly observe from the SEM images that the gap between two opposite NC tips in P3 is smaller than that in P2. Such structural difference can be accurately regulated via the well-developed EBL fabrication technique. The LSPR properties of such obtained NC patterns were further characterized via UV/vis spectrometer Lambda 20 (Perkin Elmer, Massachusetts, USA) within wavelength range of 550–1100 nm based on the transmission geometry. Fig. 2b (top) shows the experimental normalized transmission spectra upon normal incidence of the excitation source with electric field polarization parallel to the minor axis. The spectral peak positions of samples S1, P2 and P3 were experimentally observed to be 852 nm, 866 nm and 938 nm, respectively.

The theoretical transmission spectra and electric field distributions were calculated via COMSOL 4.3b commercial package. Detailed simulation parameters were described in the Supporting information. Simulated transmission spectra of the three samples were provided in the bottom of Fig. 2b. The calculated dip position under such resonant modes was found to be of 844 nm, 872 nm, and 938 nm. It could be noticed that the experimental resonant peaks were slightly deflected from the simulated results. Such mismatch may be induced by the structural difference between the real sample and the theoretical models. Furthermore, the relative broad FWHM (full width at half maximum) of the experimental spectra may be caused by the dimensional deviation of the nano-patterns raised during the fabrication process. From this perspective, good agreement can generally be concluded between the measured spectra and the simulation results.

The electric field distributions of off-resonant and on-resonant excitation wavelengths were also figured out for all three samples (Fig. 2c). The color legends show the values of the enhancement factor of the electric field, E/E_0, where E_0 is the electric field component of the illumination as described in the Supplementary information. Take S1 as an example, the strength of the electric field near the NC tips can be found to be dramatically enhanced at the wavelength (840 nm) around the resonant peak when compared to the off-resonance wavelength (560 nm). In addition, the field distributions can clearly exhibit the enhancement is mainly localized near the tips and attributed to the dipole resonance mode with electric field polarization perpendicular to the major axis (Cooper et al., 2014). Such phenomenon can also be obviously confirmed from the field distributions of the paired NC samples (P2 and P3).

2.3. Microfluidic chip-controllable concentration gradient generator

To dynamically generate concentrations for real-time detection in the microfluidic system, a concentration gradient generator was

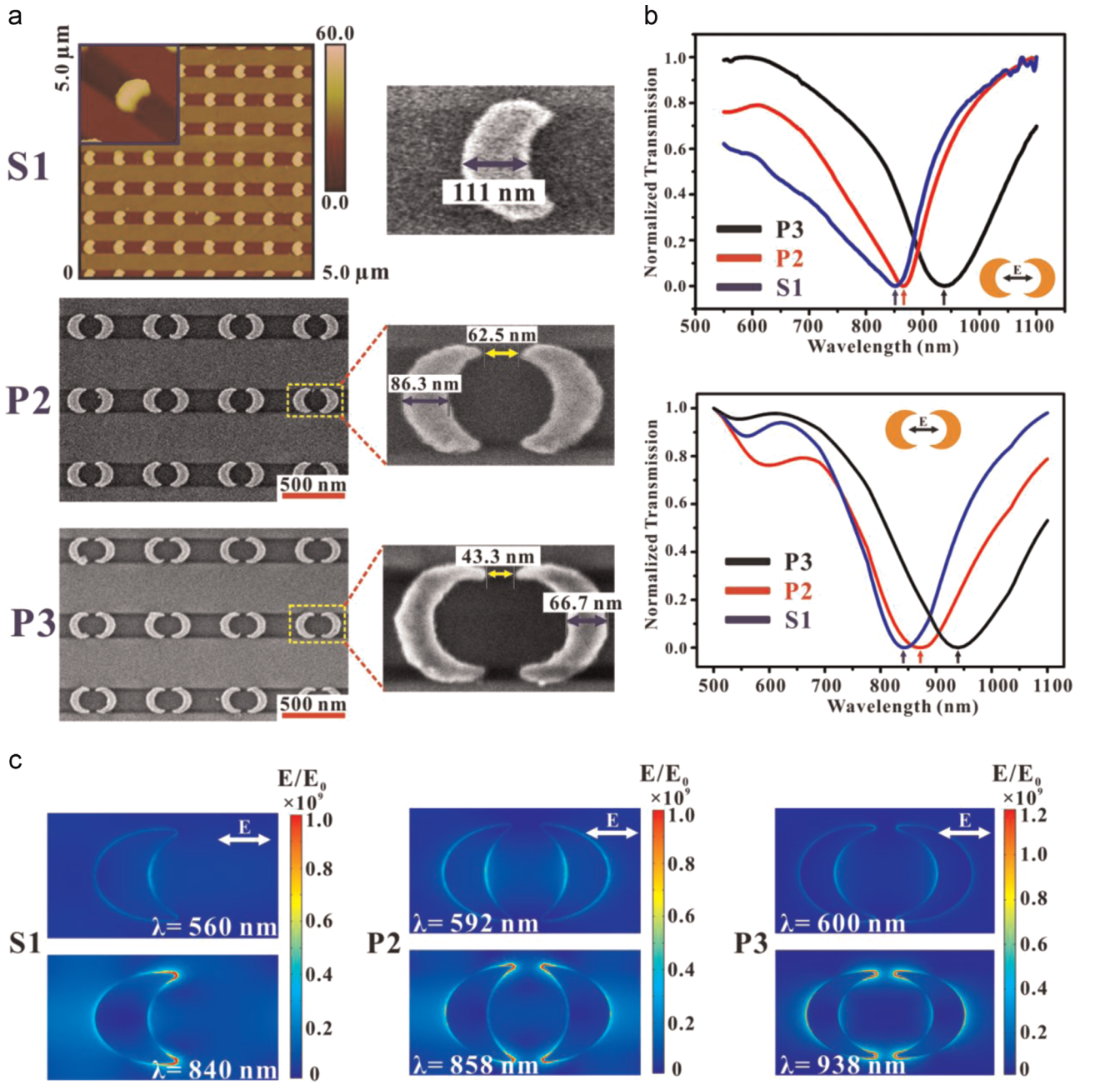

Fig. 2. (a) Atomic force microscope (AFM) images of single NC (sample S1) with enlarged scanning electron microscope (SEM) image. SEM images of paired NC (samples P2 and P3) with enlarged SEM images. The detailed dimensional values of *G* and *W* have been indicated in the corresponding positions; (b) normalized transmission spectra of single/paired NC (sample S1, P2 and P3). The top graph is the experimental result and the bottom one is the simulation result. The polarization of the incident excitation source is along the minor axis of the NC; (c) calculated near field enhancement of the three fabricated samples under resonant and non-resonant plasmonic modes. The electric field polarization (*E*) is along the minor axis which has been indicated by the arrows.

introduced in this work. Fig. 3a depicts the overall design of the microfluidic channel adopted here. The microfluidic network contains two liquid inlets (I1 and I2) and two outlets (O1 and O2). When solutions with two distinct concentrations (C_1 and C_2) flow into the microchannel, the intrinsic convective–diffusive phenomenon builds a concentration gradient among the three branches close to the outlet O2. Furthermore, via tuning the flow rate ratio between two streams (Q_1/Q_2), the particular concentration at the detection region (central branch as indicated via the yellow square) can be simply altered as presented in our previous report (Zhou et al., 2015). As a consequence, such a microfluidic layout is capable of generating dynamically controllable concentration at the desired position. Fig. 3b shows the real microfluidic chip that owns a comparable size to a Hong Kong coin. The microfluidic channel, which is patterned on a PDMS slab with depth of ~50 μm, could be produced maturely via conventional soft lithography technique as described elsewhere (Qin et al., 2010; Rogers and Nuzzo 2005). The fabrication process of the microfluidic chip was briefly presented in the Supplementary information. Red and green dye solutions were injected into the microchannel via I1 and I2 respectively with external syringe pumps (PHD2000, Harvard Apparatus, Holliston, USA). It can be clearly observed that the color of the solution at the detection region (yellow dashed circle) is different from the two adjacent branches, which reveals that mixing occurs with establishment of concentration gradients in the branches.

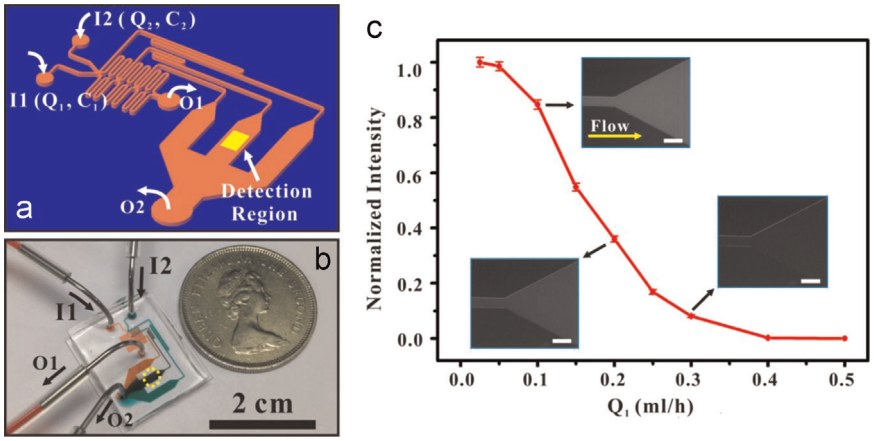

Fig. 3. (a) Overall structure of microfluidic channel for generation of dynamically controllable concentrations; (b) the sealed microfluidic chip was injected with red and green dyes to demonstrate the capability of generating concentration gradients; (c) normalized fluorescent intensity characterization of the detection region with different Q_1/Q_2. Insets are fluorescent images of the detection position with correspondence to Q_1 of 0.10 ml/h, 0.20 ml/h and 0.30 ml/h. The scale bars indicate 300 μm. (For interpretation of the references to color in this figure, the reader is referred to the web version of this article.)

To precisely characterize the dynamic concentrations at the detection region, a stream of deionized water (DI-water) and another stream of fluorescein dye ($C_{20}H_{12}O_5$, Sigma-Aldrich Co., USA) were injected into the microfluidic chip via I1 and I2, respectively. A constant flow rate of 0.10 ml/h was applied to Q_2 (fluorescein dye) while Q_1 (DI-water) was gradually increased from 0.025 ml/h to 0.50 ml/h. With different Q_1/Q_2, the fluorescent images at the detection region were taken by microscope (IX71, Olympus Corporation, Tokyo, Japan) and the corresponding gray scale intensities were analyzed via ImageJ (software version 1.47, National Institutes of Health, USA). As shown in the graph (Fig. 3c), with increased Q_1, the fluorescent intensities at the detection branch gradually decreased which means that the corresponding fluorescein concentration was successfully lowered. Such phenomenon proved that the specific analyte concentration at the detection region could be controlled via changing Q_1/Q_2. Typically, a higher value of Q_1/Q_2 will render a lower concentration in the detection position. The insets of the fluorescent images also obviously demonstrate the change of the fluorescent intensities with correspondence to the change of the flow rate of DI-water.

3. Results and discussion

3.1. Bulk refractive index (RI) sensitivity properties of NC samples

Prior to integrate the NC patterns with microfluidic gradient generator for on-chip concentration monitoring, the sensing properties of the three NC samples were systematically studied and compared. Generally, the resonance peak position of the NC patterns is sensitive to the refractive index change of the surrounding medium. Sodium chloride (NaCl) dissolved in deionized-water (DI-water) with various concentrations was prepared for determining the bulk RI sensitivity of the obtained NC samples. The NaCl concentration (w/w) in DI-water varies from 0% to 25% with corresponding RI from 1.333 to 1.3776. The sensing measurement was performed via UV/vis spectrophotometer with normal incident irradiation when the NC samples were surrounded with the aqueous medium (0–25% NaCl). The left part of Fig. 4 demonstrates the normalized transmission spectra when the NC samples were exposed to NaCl solutions with diverse concentrations. The insets provide detailed spectral profiles around the resonant wavelength area as indicated with the black dashed boxes. It should be noted that for sample P3, the peak wavelength was further determined by fitting the transmission spectra with Lorentzian function within wavelength range of 1000–1100 nm (the R^2 values of the fitting results are 0.998, 0.998, 0.997, 0.996 and 0.997 for spectra of DI-water, 5% NaCl and so forth). For all three NC sensors, we could clearly observe the red shift of resonant peak positions with increase of the NaCl concentrations and therefore increase of the RI. The resonant dip positions versus the refractive indices are plotted correspondingly as shown in the right part of Fig. 4. Numerical fitting of the three graphs presents the well linear relationship between the shift of the resonant position and the increase of the RI. A sensitivity of 195.7 nm/RIU (RIU: refractive index unit) was obtained for S1 while a higher value could be achieved with P2 of 369.2 nm/RIU. The obvious enhancement of the sensitivity may arise from a higher concentrated electric field distribution within the gaps between two individual NC. With decreased gap between two opposite NC, the highest sensitivity of ~699.2 nm/RIU was found to originate in sample P3 which owns a smaller gap of 43.3 nm between the NC tips. It can be concluded the sensing characteristics of the NC patterns can be significantly tuned via the dimensional parameters.

Figure of Merit (FOM) is another important factor to determine the capability of LSPR bio/chemical sensor (Sherry et al., 2005). FOM is defined as the ratio of the LSPR sensitivity (nm/RIU) to FWHM (nm) as given in Eq. (1). For the three samples in our work, the FWHM was found to be ~53.4 nm of S1, ~120.7 nm of P2, and ~223.8 nm for P3, respectively. Correspondingly, we can obtain the values of FOM as ~3.7 of S1, ~3.1 of P2, and ~3.1 of P3, respectively. Such FOM values are also comparable to many reported on-chip bulk plasmonic sensors (Mayer and Hafner, 2011; Petryayeva and Krull, 2011; Szunerits and Boukherroub, 2012). Future work will also try to enhance the FOM value of the NC plasmonic sensors thus improving the capability of on-chip bio/chemical sensing.

$$\mathrm{FOM} = \frac{\mathrm{Sensitivity}}{\mathrm{FWHM}} \tag{1}$$

3.2. RI measurement under fixed excitation wavelength (sample P2)

From the graphs in Fig. 4, we can also notice that the change in RI of the solution appears as intensity variations from the transmission spectra of the NC patterns. For example, in sample P2, a decrease of the normalized transmission intensity at wavelength of ~970 nm can be well observed with increase of the NaCl concentrations. Indeed, an alternative and efficient mode to detect the

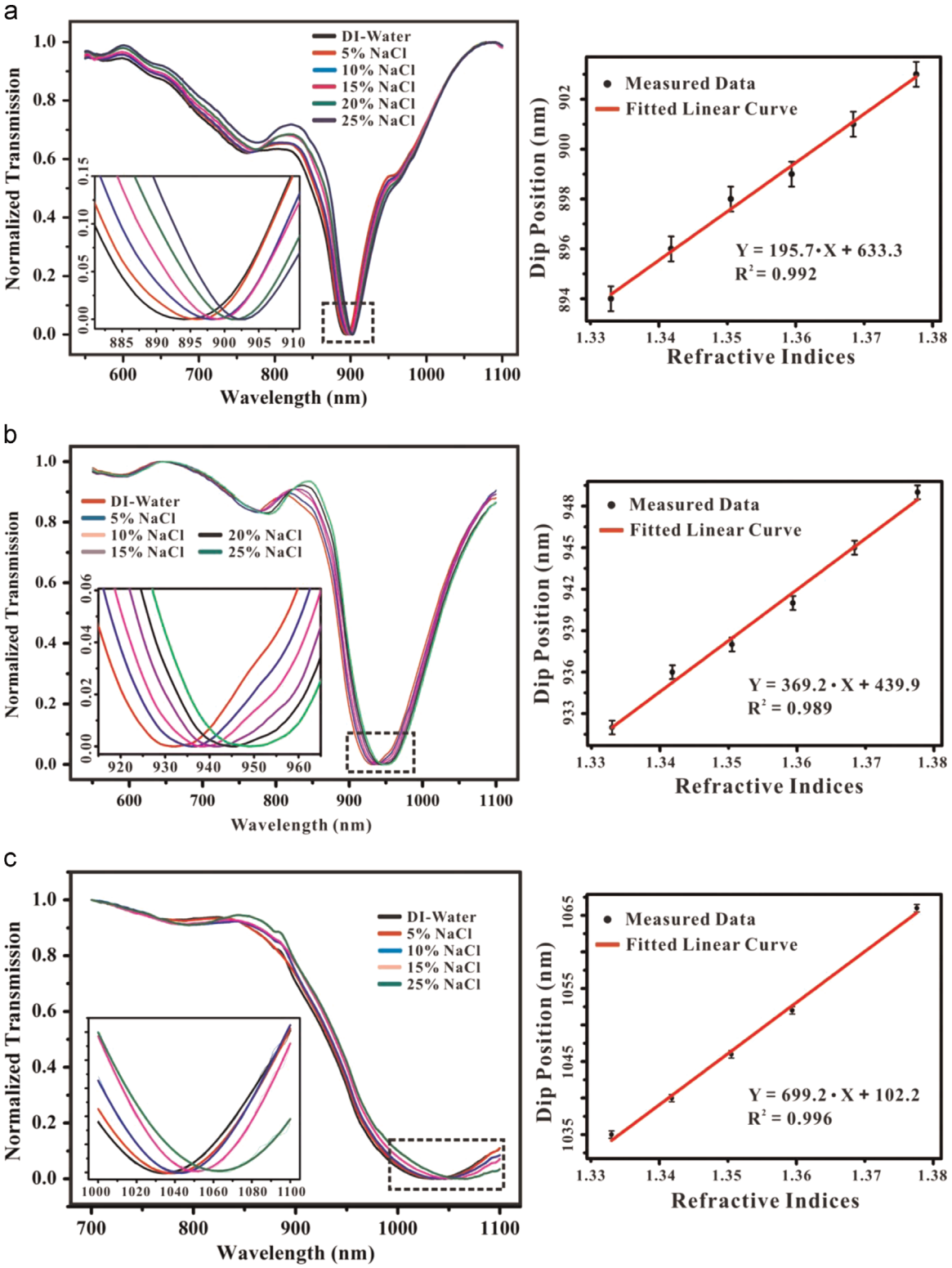

Fig. 4. Normalized transmission spectra of samples (a) S1, (b) P2, and (c) P3 surrounded in various concentrations of sodium chloride (NaCl) with different refractive indices (RIs). The insets depict the spectral regions around the dip positions (black dashed boxes) which clearly reveal the red shift of resonant wavelength with increased RIs. The right part of the figure gives the relationship between the refractive indices and the wavelength of the dip positions.

RI change was by fixing the wavelength of the excitation source while recording the variation in the intensity from the transmission spectra. The wavelength of the excitation source was therefore fixed at 970 nm, which is close to the resonant position as illustrated in Fig. 4b. For the surrounding solution of different NaCl concentrations, we monitored the transmission intensity for 5 min in order to figure out both of the sensitivity and the stability of the NC sensor.

Fig. 5a illustrates the normalized transmission intensity of sample P2 with corresponding to different NaCl concentrations at 970 nm. The average intensity for each medium has been indicated correspondingly in the figure. The maximum transmission

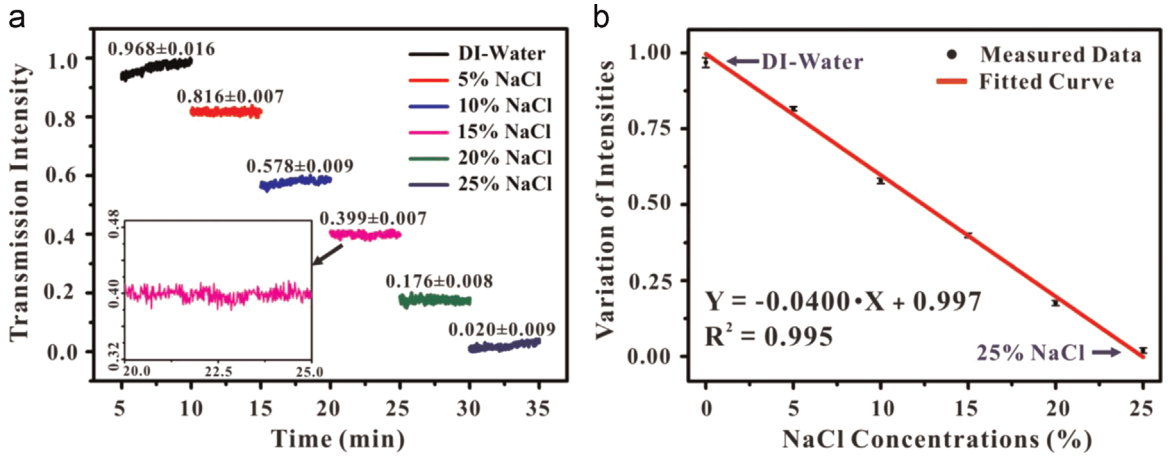

Fig. 5. (a) Experimental results of measuring the normalized intensity variations at a fixed wavelength (970 nm) of sample P2 with different concentrations of NaCl solutions. Inset: enlarged transmission intensities when the sample was immersed with 15% NaCl solution; (b) relationship between the variations of measured transmission intensities as a function of the NaCl concentrations. The fitted curve indicates the linear relation (R^2=0.995).

intensity occurred with DI-water while the minimum value arose from 25% NaCl solution (the highest concentration of the measured solutions). The inset also provides the enlarged intensity profile when P2 was immersed in 15% NaCl, which presented a high stability (standard deviation of 0.007) of the NC pattern as a RI sensor. The relationship between the NaCl concentration and the normalized transmission intensity is plotted in Fig. 5b, where the fitted curve clearly exhibited a linear relation with R^2 of 0.995. The obtained experimental results indicated the possibility of the NC pattern as a plasmonic sensor via monitoring the transmitted intensities under a fixed excitation wavelength. From the fitted formula, we can simply obtain Eq. (2) which means that the concentration of NaCl in solution can be deduced from the acquired normalized intensity. In the next section, we will

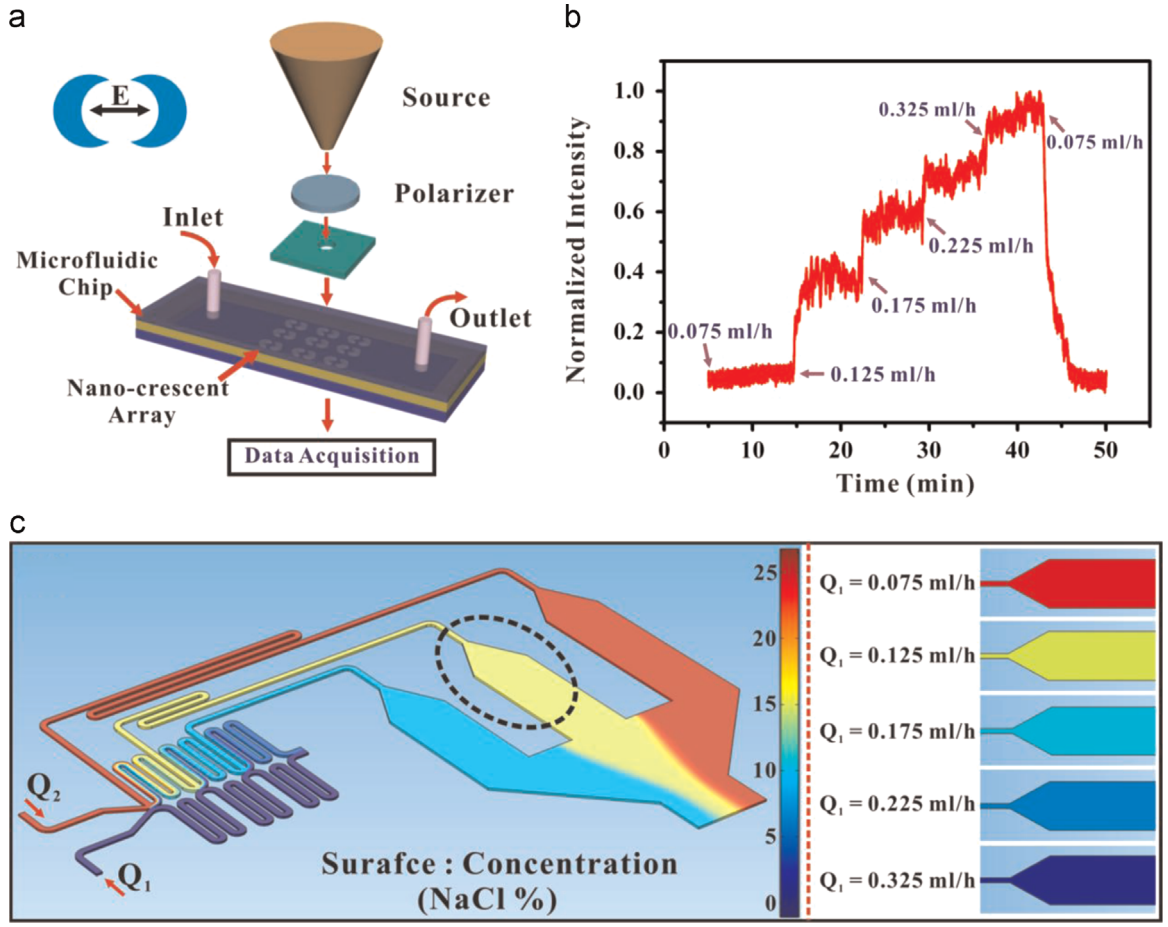

Fig. 6. (a) Experimental setup for measuring transmitted intensities with dynamically controllable NaCl concentrations at the detection region; (b) experimental transmitted intensities under different values of Q_1; the corresponding Q_1 was indicated in the graph when we changed the value of the flow rate; (c) left: 3D model for simulation of analyte concentration at the detection region (dashed ellipse) under different values of Q_1/Q_2; right: surface contours to demonstrate the specific concentration with different Q_1.

concentrate on how to monitor dynamic NaCl concentration in microfluidic gradient generator based on the NC plasmonic sensor.

$$\text{NaCl}\ (\%) = \frac{0.997 - \text{Normalized Intensity}}{0.04} \quad (2)$$

3.3. Real-time monitoring of dynamic concentration in microfluidic system

The previous section demonstrated the RI sensitivity of sample P2 via monitoring the variations of transmitted intensity with different NaCl concentrations close to the resonance. To prove the application for on-chip real-time concentration detection in a microfluidic system, P2 was integrated with the microfluidic concentration gradient generator as depicted in Fig. 3a. The quartz substrate with P2 nano-patterns was tightly bonded with another PDMS slab (with microchannel structure) after 2 min oxygen plasma surface modification. In Section 2.3, the microfluidic network has been proved to be capable of generating dynamic fluorescent concentrations at the detection region by changing the flow rate ratios between two injecting microstreams. Here we will use sample P2 as on-chip plasmonic sensor to monitor the concentration values in real-time within the microfluidic system.

The setup for real-time sensing of dynamic concentrations in microfluidic channel has been presented in Fig. 6a. Excitation wavelength of the source has been fixed at 970 nm and directed normally onto the NC detection region through a polarizer. The polarization of the electric field is parallel to the minor axis of the crescent patterns. The two inlets of the microfluidic chip have been connected to external syringe pumps (PHD 2000, Harvard Apparatus, Holliston, USA) respectively for simultaneous injection of NaCl solution and DI-water with specific flow rates. Transmitted intensity from the NC sample was then acquired and analyzed instantly via the software (UV/vis WinLab Software, Perkin Elmer, USA). To demonstrate the on-chip sensing capability of dynamic concentrations, we fixed the flow rate of NaCl concentration to be 0.10 ml/h while changed the flow rate of DI-water from 0.05 ml/h to 0.325 ml/h. Before the experiment, the transmission intensity with medium of DI-water and 25% NaCl was measured and adopted as the normalizing intensity reference of 1 and 0, respectively. As a consequence, for the NaCl concentration within range of 0 and 25%, the corresponding transmitted intensity can be normalized in range between 0 and 1.

Fig. 6b depicts the variation of the normalized intensity with respect to the change of Q_1. The micropumps were used to inject 25% NaCl solution and DI-water into the microchannel in order to generate NaCl concentration profiles in the branches. As mentioned, the NaCl concentration at the detection region can thus be swiftly modified based on Q_1/Q_2. As Q_2 was fixed at 0.1 ml/h, the expected NaCl concentration will be mainly regulated by Q_1 (DI-water). Fig. 6b clearly provides the variation of the normalized transmitted intensity which is related to the change of Q_1. For example, the transmitted intensity was normalized to be 0.050 ± 0.013 with initial Q_1 of 0.075 ml/h. When $Q_1$was further increased to 0.125 ml/h, the transmitted intensity was increased to 0.386 ± 0.032 due to the establishment of lower NaCl concentration surrounding the NC patterns under the higher Q_1/Q_2.With further increased $Q1$, we can clearly settle from the graph that a higher Q_1/Q_2 leads to a higher transmitted intensity because of the relative smaller concentration at the detection region. Finally after 42 min, we returned Q_1 to be the original value of 0.075 ml/h, and it was instantly found that the transmitted intensity quickly decreased to the initial value as provided in the graph.

To confirm the accuracy of the strategy for on-chip dynamic concentration monitoring, 3D simulation was performed to validate the NaCl concentrations under different Q_1/Q_2. Comsol Multiphysics (Version 4.3a) was adopted to model the microfluidic device with incompressible Newtonian fluid in single-phase laminar flow. The structure of the microfluid channel in simulation is identical to the real microchip as given in Fig. 6c. The color of the surface contour indicates the NaCl concentration at the specific position where deep blue means 0 and deep red means 25%. In the simulation, inlet 1 and 2 were injected with DI-water and 25% NaCl solution, respectively. The diffusion coefficient of the analyte was set of $1.6e{-}9\ m^2/s$. The flow rate of NaCl solution (Q_2) was fixed at 0.1 ml/h while Q_1 was tuned of the values as used in the experiment (0.075 ml/h, 0.125 ml/h, 0.175 ml/h, 0.225 ml/h and 0.325 ml/h). The right part of Fig. 6c provides the surface contours which indicate the corresponding concentrations under different Q_1. It can be significantly observed from the color that the NaCl concentration at the detection region gradually decreases with increased Q_1. The comparison of the NaCl concentrations between the experimental and calculated results has been provided in Table 1 in the Supplementary information. The experimental values of NaCl concentrations were deduced from Eq. (2) as the normalized transmitted intensities have been successfully recorded. Take Q_1 of 0.125 ml/h as an example, the NaCl concentration at the detection region is 15.275% from experiment and 15.132% from the simulation result, with a relative deviation of 0.95%. For other captioned flow rates, the detailed values have also been listed in Table 1. We also notice the difference between the experiment and the calculation which may derive from the various parameters in the simulation or the fluidic settings in the microfluidic system. For example, the diffusion coefficient in the model may differ slightly from the real value in the solution. Furthermore, the exact pumping rate into the microchannel may also be somehow different from the setting on the syringe pumps (the values in the simulation). Even though slight difference can be observed, our method has provided a straightforward approach to detect the concentration variation in real-time.

4. Conclusion

In summary, Au nanocrescent arrays with three different geometries were prepared via EBL and the corresponding bulk RI sensitivities were systematically investigated and compared. The highest sensitivity of ~699.2 nm/RIU was obtained via paired NC structure with closer distance between two opposite individual. We also fixed the excitation wavelength to monitor the alternation of the transmitted intensity when solutions with different RI were surrounding sample P2. It was found that the transmitted intensity linearly decreased with increased RI close to the NC surface. The obtained NC plasmonic sensor is also integrated into microfluidic system and capable of real-time monitoring the dynamic concentration variation in microchannel. The detailed concentrations from the experimental data were finally confirmed and compared with simulation results which show a good match. To conclude, we believe that such convenient and accurate method can be further well applied for lab-on-a-chip bio/chemical sensors afforded via the nanocrescent patterns.

Acknowledgment

The authors would like to acknowledge the support by Hong Kong RGC Grants HKUST 605411 and AOE/P-02/12 PG. The work was also partially supported by the Special Fund for Agro-scientific Research in the Public Interest, Ministry of Agriculture of the People's Republic of China No. 201303045. We would like to thank F. Qin and Prof. J.F. Wang from CUHK for the fruitful discussion.

Appendix A. Supplementary material

Supplementary data associated with this article can be found in the online version at http://dx.doi.org/10.1016/j.bios.2015.09.054.

References

Ahmed, T., Shimizu, T.S., Stocker, R., 2010. Nano Lett. 10 (9), 3379–3385.
Ahmed, D., Chan, C.Y., Lin, S.C., Muddana, H.S., Nama, N., Benkovic, S.J., Huang, T.J., 2013. Lab Chip 13 (3), 328–331.
Bukasov, R., Shumaker-Parry, J.S., 2007. Nano Lett. 7 (5), 1113–1118.
Bukasov, R., Ali, T.A., Nordlander, P., Shumaker-Parry, J.S., 2010. ACS Nano 4 (11), 6639–6650.
Chen, H.J., Kou, X.S., Yang, Z., Ni, W.H., Wang, J.F., 2008. Langmuir 24 (10), 5233–5237.
Cooper, C.T., Rodriguez, M., Blair, S., Shumaker-Parry, J.S., 2014. J. Phys. Chem. C 118 (2), 1167–1173.
Erickson, D., Serey, X., Chen, Y.F., Mandal, S., 2011. Lab Chip 11 (6), 995–1009.
Escobedo, C., Chou, Y.W., Rahman, M., Duan, X.B., Gordon, R., Sinto, D., Brolo, A.G., Ferreira, J., 2013. Analyst 138 (5), 1450–1458.
Estevez, M.C., Otte, M.A., Sepulveda, B., Lechuga, L.M., 2014. Anal. Chim. Acta. 806, 55–73.
Fischer, J., Vogel, N., Mohammadi, R., Butt, H., Landfester, K., Weiss, C.K., Kreiter, M., 2011. Nanoscale 3 (11), 4788–4797.
Fosser, K.A., Nuzzo, R.G., 2003. Anal. Chem. 75 (21), 5775–5782.
Gencoglu, A., Minerick, A.R., 2014. Microfluid. Nanofluid. 17 (5), 781–807.
Huang, C.J., Ye, J., Wang, S., Stakenborg, T., Lagae, L., 2012. Appl. Phys. Lett. 100, 173114.
Jeon, N.L., Dertinger, S.K.W., Chiu, D.T., Choi, I.S., Stroock, A.D., Whitesides, G.M., 2000. Langmuir 16 (22), 8311–8316.
Mannelli, I., Marco, M.P., 2010. Anal. Bioanal. Chem. 398 (6), 2451–2469.
Mayer, K.M., Hafner, J.H., 2011. Chem. Rev. 111 (6), 3828–3857.
Mensack, M.M., Wydallis, J.B., Lynn Jr., N.S., Dandy, D.S., Henry, C.S., 2013. Lab Chip 13 (2), 208–211.
Morel, M., Galas, J.C., Dahan, M., Studer, V., 2012. Lab Chip 12 (7), 1340–1346.
Pang, L., Chen, H.M., Freeman, L.M., Fainman, Y., 2012. Lab Chip 12 (19), 3543–3551.
Petryayeva, E., Krull, U.J., 2011. Anal. Chim. Acta 706 (1), 8–24.
Qin, D., Xia, Y.N., Whitesides, G.M., 2010. Nat. Protoc. 5 (3), 491–502.
Rogers, J.A., Nuzzo, R.G., 2005. Mater. Today 8 (2), 50–56.
Rycenga, M., Cobley, C.M., Zeng, J., Li, W.Y., Moran, C.H., Zhang, Q., Qin, D., Xia, Y.N., 2011. Chem. Rev. 111 (6), 3669–3712.
Schmidt, H., Hawkins, A.R., 2011. Nat. Photon. 5 (10), 598–604.
Sherry, L.J., Chang, S.H., Schatz, G.C., Duyne, R.P.V., Wiley, B.J., Xia, Y.N., 2005. Nano Lett. 5 (10), 2034–2038.
Stewart, M.E., Anderton, C.R., Thompson, L.B., Maria, J., Gray, S.K., Rogers, J.A., Nuzzo, R.G., 2008. Chem. Rev. 108 (2), 494–521.
Szunerits, S., Boukherroub, R., 2012. Chem. Commun. 48 (72), 8999–9010.
Toetsch, S., Olwell, P., Prina-Mello, A., Volkov, Y., 2009. Integr. Biol. 1 (2), 170–181.
Toma, M., Cho, K., Wood, J.B., Corn, R.M., 2014. Plasmonics 9 (4), 765–772.
Xiao, R.R., Zeng, W.J., Li, Y.T., Zou, W., Wang, L., Pei, X.F., Xie, M., Huang, W.H., 2013. Anal. Chem. 85 (16), 7842–7850.
Yoon, Y.J., Li, K.H.H., Low, Y.Z., Yoon, J., Ng, S.H., 2014. Sens. Actuator B Chem. 198, 233–238.
Zhou, B.P., Xu, W., Wang, C., Chau, Y.Y., Zeng, X.P., Zhang, X.X., Shen, R., Wen, W.J., 2015. Microfluid. Nanofluid. 18 (2), 175–184.